Vehicle-Based Mobile Mapping Test Platform: Direct Georeferencing and TLS-Based Accuracy Assessment

Rami Tamimi[1], Baris Süleymanoglu[2], Abdelgwad Elashry[3], Charles Toth[1]

[1] SPIN Laboratory, Dept. of Civil, Environmental and Geodetic Engineering, The Ohio State University, Columbus, Ohio, United States of America
[2] Faculty of Civil Engineering, Dept. of Geomatics Engineering, Yildiz Technical University, Istanbul, Türkiye
[3] School of Engineering and Computer Science, University of Hertfordshire, New Administrative Capital, Egypt

Keywords: Mobile Mapping, Direct Georeferencing, GNSS/IMU, Velodyne VLP-16, Terrestrial Laser Scanning

Abstract

Professional mobile mapping systems achieve centimeter-level accuracy through the tight integration of navigation-grade IMUs, survey-grade GNSS, and calibrated laser scanners. This paper assesses the relative and absolute accuracy of a vehicle-mounted test platform that combines a NovAtel SPAN tightly coupled GNSS/IMU with a mid-grade Velodyne VLP-16 LiDAR, evaluated along a 1.2 km test loop on The Ohio State University campus. The mobile-cloud georeferencing is driven entirely by the SPAN-processed GNSS/IMU trajectory, post-processed in NovAtel Inertial Explorer; three additional survey-grade PPK GNSS receivers are processed independently and serve as cross-checks on the trajectory. Direct georeferencing is performed in the standard ECEF formulation with per-point trajectory interpolation. An independent reference point cloud of the same area is acquired with a Leica RTC360 terrestrial laser scanner, registered and tied down to GNSS-derived ground control so that the TLS cloud carries an independent absolute geodetic datum. Absolute accuracy is then evaluated directly: identifiable features on building façades are coordinated independently in each cloud, and the coordinate differences between the mobile-cloud and TLS positions of the same features quantify the absolute georeferencing error of the directly georeferenced mobile cloud. Relative accuracy is evaluated separately from the internal geometry of each cloud: structure dimensions, inter-feature distances, and inter-feature angles are measured in the mobile cloud and in the TLS and compared, isolating the shape-preservation performance of the platform from any constant offset between the two reference frames. An auxiliary SHARE SLAM S20 handheld scanner mounted on the same vehicle is described as supplementary platform context; its data is not used in the accuracy assessment due to unreliable GNSS/IMU/SLAM integration at vehicle speeds.

1. INTRODUCTION

Mobile mapping systems (MMS) produce georeferenced 3D data using vehicle-mounted sensors, including LiDAR, cameras, and integrated GNSS/IMU navigation systems. Early implementations relied primarily on camera-based photogrammetry, whereas modern systems commonly integrate both LiDAR and imaging sensors to generate geometrically accurate and radiometrically enriched point clouds.

The concept was first demonstrated at Ohio State University with the GPSVan™ (Novak, 1995) and has matured into survey-grade commercial platforms that use navigation-grade IMU and calibrated laser scanners to reach centimeter absolute accuracy (Toth and Grejner-Brzezinska, 2004).

These high-end systems are well characterized and are not the focus of this study. Instead, this paper examines the point-cloud quality of a vehicle-mounted test platform combining a tactical-grade GNSS/IMU with a mid-grade LiDAR and identifies the primary factors that limit its point-level and feature-level accuracy.

Recent mobile mapping studies provide the context. (Elhashash et al. 2022) reviewed the field end-to-end and report that modest-cost systems reach sub-decimeter accuracy for many applications. (Kurşun 2023) achieved sub-2-dm accuracy for road-inventory mapping with a mid-grade mobile platform. (Krausková et al. 2025) report 16 cm RMSE for streambed mapping with an iPhone LiDAR. (Tamimi and Toth 2023) demonstrated centimeter-level smartphone-RTK positioning on a scooter-mounted smartphone. These studies, together with the demand for scalable 3D data from autonomous driving and digital-twin workflows (Liu et al., 2020; Guo et al., 2024; Scolamiero et al., 2025; Lyu et al., 2025), sustain continued interest in lower-cost mobile mapping.

Previous studies (e.g., Ilci and Toth, 2020) have demonstrated that centimeter-level accuracy can be achieved under similar field conditions using high-grade navigation systems and multi-LiDAR configurations. This study evaluates a single forward-facing LiDAR setup against a terrestrial-laser-scanner reference, in line with that earlier work but at a lower hardware tier.

The principal contribution of this paper is a quantitative absolute- and relative-accuracy characterization of the directly georeferenced mobile cloud against an independently georeferenced TLS reference. The remainder of the paper is organized as follows: Section 2 describes the platform and test loop, Section 3 covers trajectory processing and direct georeferencing, Section 4 presents the accuracy results, and Section 5 concludes.

2. PLATFORM AND DATA

2.1 Vehicle and Sensor Configuration

The mapping platform is a 2026 Tesla Model Y with a roof-mounted sensor bar carrying two Velodyne VLP-16 LiDAR units (front-facing and rear-facing, 10 Hz, 16 beams, ±3 cm range precision per manufacturer), three survey-grade PPK GNSS receivers (Emlid Reach RS3 at 5 Hz, Emlid Reach RS4 Pro at 5 Hz, Septentrio PolaRx5 at 1 Hz), and a NovAtel SPAN tightly-coupled GNSS/IMU system (INSPVAX at 200 Hz, RAWIMUSX at 125 Hz). The data analyzed in this paper come from the front VLP-16. Figure 1 shows the sensors attached to the vehicle.

Sensor positions were measured in the vehicle body frame (origin at the SPAN IMU marked reference, X forward, Y left, Z up). The front VLP-16 lever arm was further verified against the lever-arm value applied by Inertial Explorer during SPAN post-processing. Body-frame coordinates are reported in Table 1.

The four GNSS antennas share a common Y offset of 0.076 m and are distributed along the X-axis of the body frame. Platform attitude is provided by the tightly integrated SPAN GNSS/IMU solution; the three additional PPK receivers serve as independent cross-checks on the SPAN trajectory.

https://doi.org/10.5194/isprs-archives-XLIX-B1-2026-49-2026 |

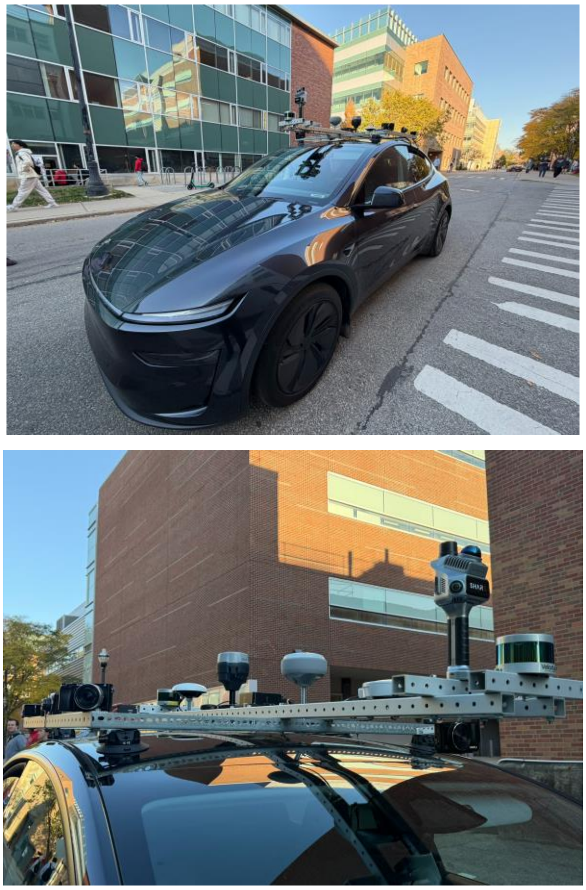

Figure 1. Tesla Model Y with a roof-mounted sensor bar

.

Table 1. Sensor body-frame coordinates, origin at SPAN IMU.

Sensor	Y (m)	X (m)	Z (m)
NovAtel SPAN GNSS	0.076	0.648	−0.005
Emlid Reach RS4 Pro	0.076	0.267	0.050
Emlid Reach RS3	0.076	−0.191	0.065
Septentrio PolaRx5	0.076	−0.572	0.055
VLP-16 (front)	0.076	1.067	0.023
VLP-16 (back)	0.076	−0.800	0.023
Livox MID-360	0.076	0.914	0.023

The body-frame coordinates were cross-checked against PPK-derived baselines averaged over a 140 s common-static window before the drive (UTC 19:08:51 – 19:11:11). Agreement with the surveyed values is at the millimeter level: RS4–RS3 differs by −2.3 mm (0.4559 m PPK vs. 0.4582 m surveyed), RS3–Septentrio by −1.6 mm (0.3796 m vs. 0.3811 m), and RS4–Septentrio by −4.1 mm (0.8349 m vs. 0.8390 m). The PPK baseline length is stable to 1.5–2.1 mm (1σ) across the window for all three pairs, confirming that the surveyed sensor geometry is consistent with the GNSS solution to within the noise floor of the receivers themselves.

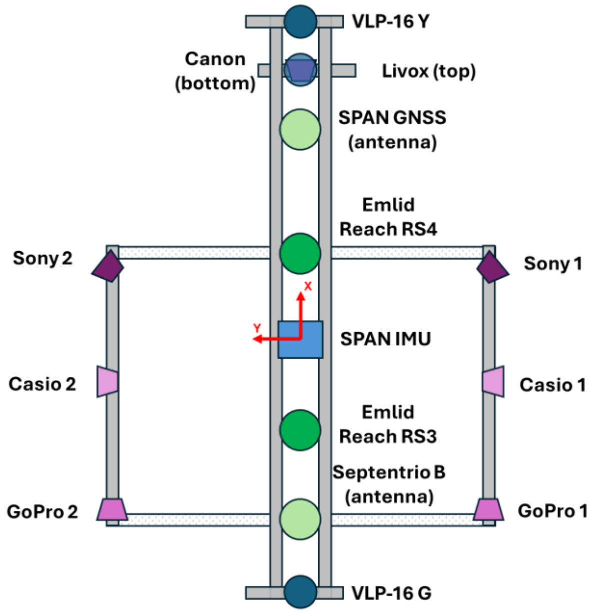

Figure 2. Platform configuration

2.2 Test loop

Data were collected along a 1.2 km loop around Bolz Hall on The Ohio State University campus. The trajectory passes through open-sky, tree-canopy, and building-adjacent segments. The vehicle averaged 4.25 m s^{-1}, and the front-mounted VLP-16 produced 5,101 frames over the loop. The tightly coupled GNSS/IMU data is shown in Figure 3.

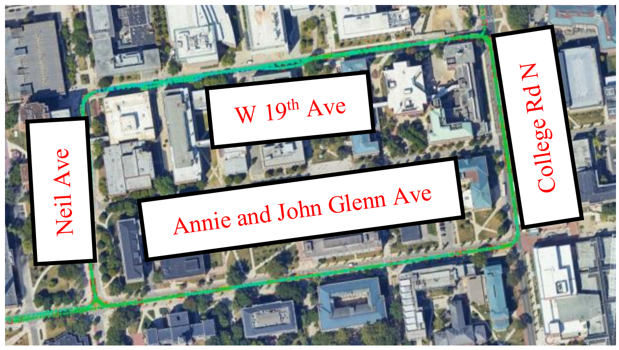

Figure 3. 1.2 km test site on Neil Ave, Annie and John Glenn Ave, College Road N, and W 19th Ave on the OSU Campus

2.3 Reference Point Cloud Generation with Leica RTC360

The reference cloud was acquired with a Leica RTC360 terrestrial laser scanner (TLS), with a sampling rate of up to 2 million points per second over a measurement range of 0.5–130 m. The manufacturer-specified range accuracy is ± (1.0 mm + 10 ppm) over this range, with a beam divergence of 0.5 mrad and a beam diameter of 6 mm at the exit window (Leica RTC360, 2018). Individual scans were registered using the Leica Register 360 software (Bauer, 2024). Figure 4 shows the georeferenced TLS point cloud.

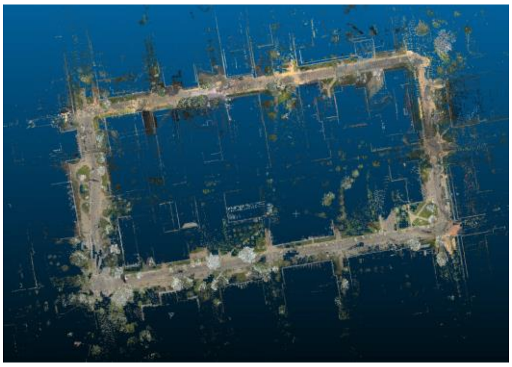

Figure 4. Leica RTC360 point cloud with GNSS controlled georeferencing

2.4 SHARE SLAM S20 scanner system

A SHARE SLAM S20 handheld SLAM scanner, equipped with a Livox MID-360 LiDAR (40 beams, 360° × 59° field of view, ± 2 cm range precision), an integrated RTK GNSS receiver, and an integrated IMU, was mounted on the test vehicle alongside the primary sensor bar and operated over the same loop. The SHARE is a consumer-grade handheld unit designed for pedestrian-paced indoors and short-range outdoor capture, with its onboard GNSS and IMU intended as auxiliary aids to a primary SLAM-based georeferencing pipeline. In this study it was operated outside its intended use case to evaluate whether a handheld system of this class could be repurposed as a low-cost mobile mapping platform.

In practice, the system's onboard integration of the RTK GNSS and IMU with the SLAM solution proved unreliable at vehicle speeds using the current available software. The sessions defaulted to a SLAM-only trajectory and exhibited noticeable positional drift over the length of the loop or failed outright. The SHARE point cloud is therefore not used in any of the accuracy assessments of Section 4. As consumer-grade handheld SLAM units continue to mature and their GNSS/IMU/SLAM integration becomes more robust at vehicle speeds, future work may revisit this comparison once the data can be reliably georeferenced.

3. MATERIALS AND METHODS

3.1 Trajectory Post-processing and Georeferencing

Raw NovAtel SPAN IMU observations and raw GNSS observations were processed in NovAtel Inertial Explorer against a local base station using a tightly coupled GNSS/IMU engine in a forward-plus-reverse combined (smoothed) run. Ambiguity resolution was set to fix-and-hold with a 10° elevation mask, and zero-velocity updates were applied over stationary intervals exceeding 30 s. The mean horizontal standard deviation reported by Inertial Explorer is approximately 1 cm, with a maximum of 5.7 cm; only about 0.2 % of epochs exceed 5 cm. Narrow-integer ambiguity fix was maintained across the entire loop, as the integrated IMU absorbs the short-duration GNSS degradations that would otherwise break a stand-alone PPK solution.

The three stand-alone PPK streams serve as independent cross-checks on the SPAN trajectory. The Emlid RS3 (5 Hz) and Septentrio PolaRx5 (1 Hz) achieved narrow-integer ambiguity fix on 90.5 % and 80.9 % of kinematic epochs respectively; the Emlid RS4 Pro (5 Hz) reached 93.8 % but, as noted in Section 2.1, was logged only over the stationary initialization and so is not directly comparable to the two kinematic streams. Epochs that drop from a fixed solution typically degrade to float or single-point positioning and concentrate in the tree-canopy and building-multipath segments of the loop.

The forward-only and reverse-only Inertial Explorer solutions agree at the millimeter level over the fixed-ambiguity epochs, indicating that the reported standard deviation reflects the actual trajectory precision rather than an optimistic Kalman-filter estimate.

3.2 Direct Georeferencing Approach

The standard direct georeferencing equation (Toth and Grejner-Brzezinska, 2004) is used in its ECEF form:

$$p\_ECEF(t) = p\_IMU\_ECEF(t) + R\_ECEF{\leftarrow}body(t) \cdot [\, R\_boresight \cdot p\_sensor + \ell\,] \quad (1)$$

where p_sensor is a LiDAR return expressed in the sensor frame at emission time t, ℓ is the lever arm from the IMU to the LiDAR origin (Table 1), R_boresight is the static sensor-to-body rotation, and R_ECEF←body(t) is the body-to-ECEF rotation assembled from the roll, pitch, and heading of the SPAN solution interpolated to t. Each return is time-tagged and transformed independently; no per-frame constant-pose approximation is used.

3.3 Point Cloud Generation

Equation (1) was implemented in custom Python software. The SBET is the source of position and attitude for the georeferencing. Each LiDAR return retains the GPS time at which it was emitted, and the trajectory is interpolated to that time on a per-point basis: position by linear interpolation between adjacent SBET epochs, and attitude by spherical linear interpolation (slerp) on the quaternion form of the body-to-ECEF rotation. The 200 Hz IMU rate of the SBET means each LiDAR return falls within a 5 ms interpolation window, over which the trajectory is effectively linear.

The lever arm and boresight rotation are applied to each return in the sensor frame before the rotation into ECEF, so the sensor-frame point, the lever arm, the boresight, and the trajectory pose are all consumed in a single transformation rather than as a sequence of intermediate clouds. The geometry of the output cloud is determined entirely by the SPAN/IMU-derived trajectory and the surveyed sensor geometry. Figure 5 shows the point cloud generated from the mobile mapping system.

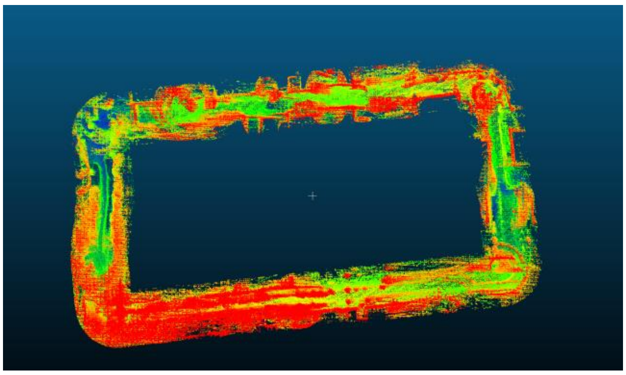

Figure 5. Direct-georeferenced point cloud from mobile mapping system.

https://doi.org/10.5194/isprs-archives-XLIX-B1-2026-49-2026 |

4. RESULTS

4.1 Surface noise

Surface noise was evaluated on building façades along the loop using cross-section profiling in Pix4Dmatic. For each of ten façade locations distributed across the test area, a 10 cm-deep section box of approximately 14 m × 14 m extent was placed flush against the wall. The points falling within the section were viewed edge-on so that the wall surface appears as a thin band; the band's thickness in the wall-normal direction is the plane-orthogonal scatter of the cloud at that location. The same section geometry was applied to both the mobile cloud and the TLS reference at each wall so that the two clouds were sampled over identical volumes.

Across the ten cross-sections, the mobile cloud's plane-orthogonal scatter has a median width of 30.5 cm, with values ranging from 24.4 cm to 45.7 cm. The TLS reference, sampled through the same section boxes, has a median scatter width of 4.9 cm, ranging from 4.6 cm to 5.3 cm. Per-wall results are reported in Table 2.

Table 2. Plane-orthogonal scatter of the mobile cloud and TLS reference, measured at ten façade cross-sections distributed across the loop. Each value is the band thickness measured edge-on through a 10 cm-deep section box placed at the wall.

Wall	Segment	Mobile (cm)	TLS (cm)
1	Open Sky	24.4	4.7
2	Open Sky	27.1	4.9
3	Open Sky	26.5	4.6
4	Open Sky	28.9	5.0
5	Tree Canopy	30.2	4.8
6	Tree Canopy	31.7	5.1
7	Tree Canopy	33.8	4.9
8	Corridor	35.6	5.0
9	Corridor	41.3	4.8
10	Corridor	45.7	5.3
Median		30.5	4.9
Range		24.4-45.7	4.6-5.3

The TLS scatter is constant across all ten walls, varying by less than 1 cm regardless of segment since the TLS is ground-based and its georeferencing is independent of any vehicle trajectory. The mobile-cloud scatter, by contrast, varies systematically with segment type. On walls in open-sky portions of the loop (walls 1–4) the mobile scatter is 24.4–28.9 cm. On walls in tree-canopy segments (walls 5–7) it broadens to 30.2–33.8 cm. On walls in the building-multipath segment along Neil Avenue (walls 8–10) it broadens further to 35.6–45.7 cm. The relationship between segment quality and mobile-cloud scatter is monotonic, localizing the GNSS-driven degradation already identified in the trajectory analysis of Section 3.1 and confirming that the mobile-cloud noise floor is dominated by trajectory-coupled terms rather than by LiDAR alone.

The factor-of-six difference between the two clouds at the median, and the factor-of-nine difference at the worst Neil Avenue wall, reflects multiple terms in the mobile-cloud error budget. The VLP-16's manufacturer-specified ± 3 cm range precision contributes only a small fraction of the observed scatter. The remainder accumulates from residual boresight and lever-arm error, per-point trajectory interpolation, scan-line stitching across the 100 ms LiDAR rotation period during which the platform translates approximately 42 cm at the loop's mean speed, and IMU attitude noise propagating through the rotation into the wall-normal direction. The TLS, sampling the same wall from a static tripod-mounted setup, is subject only to its specified ± (1.0 mm + 10 ppm) range precision and is therefore an order of magnitude tighter at the point level.

Figure 6 shows a representative cross-section pair. The mobile cloud appears as a 30 cm-wide band running horizontally across the section view; the TLS reference appears as a tighter 5 cm band with discrete offsets at window frames and recessed features. Both bands are sampled at the same wall, through the same 10 cm slice volume, with no further filtering or processing applied. Figure 7 shows the same comparison at a wall within the Neil Avenue corridor, where the mobile-cloud band broadens to 45 cm while the TLS band remains near 5 cm.

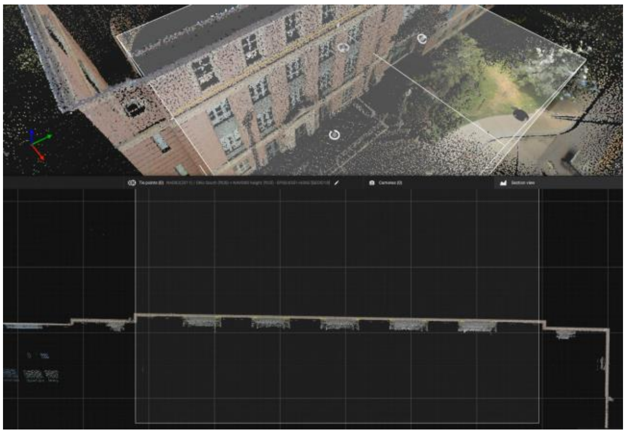

Figure 6. Cross-section pair at a wall with Leica RTC360

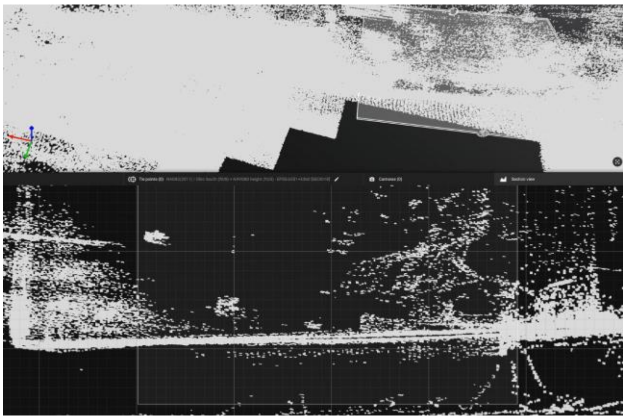

Figure 7. Cross-section pair at a wall with VLP-16

The cross-section measures the raw point-level noise of the directly georeferenced cloud, including all trajectory and calibration contributions. This raw scatter is the noise floor that the cloud carries at the *individual point* level. The accuracy assessments in Section 4.2 are conducted on identifiable architectural features rather than on individual points; for a feature defined by tens to hundreds of nearby points, the centroid is determined more tightly than the underlying point scatter would suggest, which is why the absolute and relative accuracies

https://doi.org/10.5194/isprs-archives-XLIX-B1-2026-49-2026 | © Author(s) 2026. CC BY 4.0 License.

reported in Section 4.2 land in the 5–10 cm and 2–3 cm bands rather than at the 30 cm cross-section width.

4.2 Comparison with the TLS reference

The TLS reference is referenced to NAD83(2011) Ohio South (ftUS) horizontally and NAVD88 (GEOID18) vertically. The mobile cloud, internally referenced through the SPAN trajectory, is reprojected into the same frame for comparison; this is a geodetic transformation only and does not alter the internal geometry of the cloud. The accuracy assessment is built on a set of identifiable check features distributed along the loop — building corners, door frames, window mullions, and other sharp architectural details that can be located unambiguously in both clouds. Each feature is coordinated independently in each cloud by manual point selection in CloudCompare, repeated three times, and averaged. The repeatability of the manual selection is 1.0–1.5 cm in the mobile cloud and 0.5 cm in the TLS, consistent with the surface-noise floor of Section 4.1 and the point density of each cloud.

4.2.1 Absolute accuracy. 25 features were coordinated in both clouds. For each, the absolute coordinate difference $\Delta = (X\_TLS - X\_mob, Y\_TLS - Y\_mob, Z\_TLS - Z\_mob)$ was computed (Table 3). The median absolute 3D difference is 6.4 cm, with horizontal and vertical components of 5.1 cm and 3.8 cm respectively; 18 of the 25 features fall below 8 cm in 3D. The five tightest features agree to 1.8, 2.4, 3.0, 3.2, and 3.5 cm. The remaining seven features cluster in the Neil Avenue corridor, where mature tree canopy and tall building frontage drop the independent PPK streams to float (Section 3.1) and 3D differences rise to 11–18 cm.

This 5–10 cm absolute-accuracy band is the expected outcome of the platform's error budget: the SPAN trajectory contributes ~1 cm horizontal standard deviation, the VLP-16 ~3 cm range noise, and the manual-pick repeatability another 1–2 cm. Decimeter-level residuals on the Neil Avenue features are bounded in time and space rather than propagated through the loop, because the SPAN IMU bridges the GNSS gaps and prevents trajectory error from accumulating beyond the duration of each gap.

Table 3. Absolute coordinate differences between identifiable check features in the mobile cloud and the TLS reference, by trajectory segment.

Segment	Points	MedianΔ3D (cm)	MaxΔ3D (cm)
Open Sky	12	4.6	8.9
Tree Canopy	6	6.2	11.1
Neil Avenue	7	13.2	18.6
Overall	25	6.4	18.6

4.2.2 Relative accuracy. Inter-feature distances were computed between selected pairs of check features in each cloud independently, and the differences $\Delta D = D\_mob - D\_TLS$ are reported per baseline length in Table 4. Fifteen pairs were measured, with most concentrated at short baselines were multiple coordinatable features cluster on adjacent building frontage. The median absolute distance difference is 2.5 cm and the 90th percentile is 6.8 cm. On pairs where both endpoints fall within open-sky segments, the median $|\Delta D|$ tightens to 1.8 cm — at or below the surface-noise floor of Section 4.1. On pairs where one or both endpoints fall within the Neil Avenue corridor, the median $|\Delta D|$ broadens to 7.9 cm, again localizing the GNSS-driven degradation.

Table 4. Inter-feature distance preservation between the mobile cloud and the TLS reference, by baseline length. *ΔD* is the difference between the distance measured in the mobile cloud and the same distance measured in the TLS, computed independently in each cloud.

Baseline (m)	n pairs	MedianΔD (cm)	MaxΔD (cm)
0-50	9	2.1	6.8
50-150	4	3.0	7.4
150-300	2	3.6	8.1
All pairs	15	2.5	8.1

5. CONCLUSION

A vehicle-based mobile mapping test platform combining a NovAtel SPAN tightly coupled GNSS/IMU, and a Velodyne VLP-16 LiDAR has been characterized along a 1.2 km loop at The Ohio State University. Raw GNSS and IMU observations were post-processed in NovAtel Inertial Explorer using a tightly coupled forward-plus-reverse smoothed solution, producing a trajectory with a mean horizontal standard deviation of approximately 1 cm. The point cloud was generated by direct georeferencing in the standard ECEF formulation, with each LiDAR return time-tagged and transformed independently against the per-point-interpolated trajectory. No SLAM or post-hoc refinement was applied.

Cross-section profiling across ten façade locations along the loop measured a median plane-orthogonal scatter of 30.5 cm in the mobile cloud against 4.9 cm in the TLS reference. The mobile-cloud scatter varies monotonically with segment type — 24–29 cm in open-sky portions, 30–34 cm in tree canopy, and 36–46 cm in the Neil Avenue building corridor — while the TLS scatter is constant to within 1 cm across all ten walls regardless of segment. The directly georeferenced cloud's raw point-level noise is therefore dominated by trajectory-coupled terms (residual calibration error, per-point interpolation, scan-line stitching, IMU attitude noise) rather than by LiDAR range precision alone. Compared against the TLS reference on 25 identifiable check features, the mobile cloud agrees at a median 3D difference of 6.4 cm, tightening to 4–5 cm in open-sky segments and broadening to 13–18 cm along the Neil Avenue corridor. Internal scale and shape are preserved at the 2–3 cm level across all tested baselines. The factor-of-ten difference between the per-point cross-section scatter and the per-feature absolute accuracy reflects the centroid averaging of many points within each feature; both metrics localize the same GNSS-driven degradation in the same segment of the loop, and both sit within the expected performance envelope for a tactical-grade GNSS/IMU paired with a mid-grade rotating LiDAR.

Future work will extend the pipeline with a LiDAR-SLAM augmentation layer with two roles: bridging the trajectory through GNSS-degraded segments such as the Neil Avenue corridor identified here and tightening inter-frame consistency in the directly georeferenced cloud to reduce the trajectory-coupled scatter and recover some of the crisp surface geometry visible in the TLS reference. The SHARE SLAM S20 dataset described in Section 2.4 will also be revisited once the system's onboard GNSS/IMU/SLAM integration becomes more robust at vehicle speeds, at which point a meaningful evaluation of how a handheld scanner of that class performs in a vehicle-mounted role will become possible.

https://doi.org/10.5194/isprs-archives-XLIX-B1-2026-49-2026 | © Author(s) 2026. CC BY 4.0 License.

ACKNOWLEDGEMENTS

This research was supported by the SPIN Laboratory at The Ohio State University. The authors thank the Department of Civil, Environmental and Geodetic Engineering for access to the survey-grade GNSS and IMU equipment used in this study. The authors also thank NOAR Technologies for access to the Leica RTC360 and Register 360, Pix4D for their software, and the team at SHARE for access to the SLAM S20 scanner.

REFERENCES

Bauer, P., Woschitz, H., 2024: Laboratory Investigations of the Leica RTC360 Laser Scanner—Distance Measuring Performance. Sensors, 24(12), 3742.

Elhashash, M., Albanwan, H., Qin, R., 2022: A review of mobile mapping systems: From sensors to applications. Sensors, 22(11), 4262.

Elghazaly, G., Frank, R., Harvey, S., Safko, S., 2023: High-Definition Maps: Comprehensive Survey, Challenges, and Future Perspectives. IEEE Open J. Intell. Transp. Syst., 4, 527–550.

Guo, X., Cao, Y., Zhou, J., Huang, Y., Li, B., 2023: HDM-RRT: A fast HD-map-guided motion planning algorithm for autonomous driving in the campus environment. Remote Sens., 15(2), 487.

Guo, Y., Zhou, J., Li, X., Tang, Y., Lv, Z., 2024: A Review of Crowdsourcing Update Methods for High-Definition Maps. ISPRS Int. J. Geo-Inf., 13(3), 104.

Ilci, V., Toth, C., 2020: High-definition 3D map creation using GNSS/IMU/LiDAR sensor integration to support autonomous vehicle navigation. Sensors, 20(3), 899.

Krausková, D., Mikita, T., Hrůza, P., Kudrnová, B., 2025: Accuracy assessment of iPhone LiDAR for mapping streambeds and small water structures in forested terrain. Sensors, 25(19), 6141.

Kurşun, H., 2023: Accuracy comparison of mobile mapping system for road inventory. Mersin Photogramm. J., 5(2), 55–66.

Leica. Leica RTC360; User Manual, Version 1.0., 870891-1.0.1en; Leica Geosystems AG: Heerbrugg, Switzerland, 2018.

Liu, R., Wang, J., Zhang, B., 2020: High-definition map for automated driving: Overview and analysis. J. Navig., 73(2), 324–341.

Lyu, H., Berrio Perez, J. S., Huang, Y., Li, K., Shan, M., Worrall, S., 2025: Online High-Definition Map Construction for Autonomous Vehicles: A Comprehensive Survey. J. Sensor Actuator Netw., 14(1), 15.

Novak, K., 1995: Mobile mapping technology for GIS data collection. Photogramm. Eng. Remote Sens., 61(5), 493–501.

Peng, C. W., Hsu, C. C., Wang, W. Y., 2020: Cost effective mobile mapping system for color point cloud reconstruction. Sensors, 20(22), 6536.

Scolamiero, V., Boccardo, P., La Riccia, L., 2025: Mobile Mapping System for Urban Infrastructure Monitoring: Digital Twin Implementation in Road Asset Management. Land, 14(3), 597.

Süleymanoglu, B., Tamimi, R., Yilmaz, Y., Soycan, M., Toth, C., 2023: Road infrastructure mapping by using iPhone 14 Pro: An accuracy assessment. Int. Arch. Photogramm. Remote Sens. Spatial Inf. Sci., 48, 347–353.

Tamimi, R., Toth, C., 2023: Performance Assessment of a Mini Mobile Mapping System: iPhone 14 Pro Installed on an E-Scooter. Int. Arch. Photogramm. Remote Sens. Spatial Inf. Sci., 48, 307–315.

Toth, C., Grejner-Brzezinska, D., 2004: Redefining the Paradigm of Modern Mobile Mapping. Photogramm. Eng. Remote Sens., 70(6), 685–6